Observation of an anti-damping spin-orbit torque originating from the Berry curvature

H. Kurebayashi,[1,2,*] Jairo Sinova,[3,4,5] D. Fang,[1] A. C. Irvine,[1] T. D. Skinner,[1] J. Wunderlich,[5,6] V. Novák,[5] R. P. Campion,[7] B. L. Gallagher,[7] E. K. Vehstedt,[4,5] L. P. Zârbo,[5] K. Výborný,[5] A. J. Ferguson,[1,†] and T. Jungwirth[5,7]

[1]*Microelectronics Group, Cavendish Laboratory, University of Cambridge, CB3 0HE, UK*

[2]*PRESTO, Japan Science and Technology Agency, Kawaguchi 332-0012, Japan*

[3]*Institut für Physik, Johannes Gutenberg-Universität Mainz, 55128 Mainz, Germany*

[4]*Department of Physics, Texas A&M University, College Station, Texas 77843-4242, USA*

[5]*Institute of Physics ASCR, v.v.i., Cukrovarnická 10, 162 53 Praha 6, Czech Republic*

[6]*Hitachi Cambridge Laboratory, Cambridge CB3 0HE, UK*

[7]*School of Physics and Astronomy, University of Nottingham, Nottingham NG7 2RD, UK*

(Dated: January 15, 2014)

Magnetization switching at the interface between ferromagnetic and paramagnetic metals controlled by current-induced torques could be exploited in magnetic memory technologies. Compelling questions arise on the role played in the switching by the spin-Hall effect in the paramagnet and by the spin-orbit torque originating from the broken inversion symmetry at the interface. Of particular importance are the anti-damping components of these current-induced torques acting against the equilibrium-restoring Gilbert damping of the magnetization dynamics. Here we report the observation of an anti-damping spin-orbit torque that stems from the Berry curvature, in analogy to the origin of the intrinsic spin-Hall effect. We chose the ferromagnetic semiconductor (Ga,Mn)As as a material system because its crystal inversion asymmetry allows us to measure bare ferromagnetic films, rather than ferromagnetic/paramagnetic heterostructures, eliminating by design any spin-Hall effect contribution. We provide an intuitive picture of the Berry curvature origin of this anti-damping spin-orbit torque and its microscopic modelling. We expect the Berry curvature spin-orbit torque to be of comparable strength to the spin-Hall effect-driven anti-damping torque in ferromagnets interfaced with paramagnets with strong intrinsic spin-Hall effect.

In one interpretation discussed in the literature to date, the current induced switching at the ferromagnet/paramagnet interfaces[1,2] originates from an anti-damping component of the spin-orbit torque (SOT)[1,3–24] at the broken space-inversion-symmetry interface, and in another,[2,23,25] the spin-Hall effect (SHE)[26–32] in the paramagnet combines with the anti-damping spin-transfer torque (STT)[33–36] in the ferromagnet. Because to date the theories have considered a scattering-related SOT whose anti-damping component is expected to be relatively weak compared to the field-like SOT component,[18,19] much attention has been drawn to the SHE-STT interpretation, in which the large SHE originates from the Berry curvature in the band structure of a clean crystal.[2,28,29,37] The focus of the present work is on a large anti-damping SOT that stems from an analogous Berry curvature origin to the intrinsic SHE.

In the usual semiclassical transport theory, the linear response of the carrier system to the applied electric field is described by the non-equilibrium distribution function of carrier eigenstates which are considered to be unperturbed by the electric field. The form of the non-equilibrium distribution function is obtained by accounting for the combined effects of the carrier acceleration in the field and of scattering. For the SOT, the non-equilibrium distribution function can be used to evaluate the current induced carrier spin-density which then exerts the torque on the magnetization via the carrier – magnetic moment exchange coupling. The field-like component of the SOT reported in the previous theoretical and experimental studies in (Ga,Mn)As films[4,8,9,11,24] and predicted for interfaces with broken structural inversion symmetry[5,6] is described within this theory framework. Scattering related mechanisms were also considered to generate an anti-damping like component of the SOT in the transition-metal multilayers.[17–20] In Ref. 17, the anti-damping like SOT term arises from the electron-scattering induced spin relaxation. Ref. 20 employed the semiclassical diffusion formalism while in Refs. 18,19 the anti-damping like SOT is obtained within a quantum kinetic formalism and ascribed to spin-dependent carrier lifetimes[18] or to a term arising from the weak-diffusion limit which in the leading order is proportional to a constant carrier lifetime.[19] Ref. 18 also recalls the connection between these scattering-related anti-damping SOT theories and the out-of-plane spin polarization resulting from the interplay between spin-orbit interaction and external electric and magnetic fields in a non-magnetic 2D Rashba system in the presence of anisotropic impurity scattering.[38]

Unlike the transport theories based on evaluating the non-equilibrium distribution function, in the time-dependent quantum-mechanical perturbation theory the linear response is described by the equilibrium distribution function and by the perturbation of carrier wavefunctions in the applied electric field. This latter framework was the basis of the intrinsic Berry curvature mechanism introduced to explain the anomalous Hall effect originally in ferromagnetic semiconductor (Ga,Mn)As[39] and, subsequently, also in a number of common transition metal ferromagnets.[40] Via the anomalous Hall effect, the Berry curvature physics entered the field of the SHE where again studies initially focused on the spin-orbit coupled semiconductor structures due to their relatively simple band structure and, subsequently, included the spin-orbit coupled metal paramagnets. Here the concept of a scattering-independent origin brought the attention of a wide physics community to this relativistic phenomenon, eventually turning the SHE into an important field of condensed matter physics and spintronics.[32]

In recent experiments it has been argued that the intrinsic SHE[2,28,29,37] combined with the STT explains the symmetry and approximate magnitude of the observed in-plane current-induced magnetization switching at the ferromagnet/paramagnet metal interfaces. Here we demonstrate that there exists an intrinsic anti-damping SOT that has the relativistic quantum-mechanical Berry curvature origin as the intrinsic SHE. In this initial study of the intrinsic anti-damping SOT we focus on (Ga,Mn)As, taking advantage again of the strong spin-orbit coupling and simple band structure of this ferromagnetic semiconductor. In case of the SOT, (Ga,Mn)As provides yet another essential advantage, compared to e.g. common metals, allowing us to readily isolate this new SOT from the SHE-STT mechanism. The zinc-blende crystal structure of (Ga,Mn)As lacks bulk space-inversion symmetry which makes it possible to study the SOT phenomena in a bare ferromagnetic semiconductor film.[8,10,11] Since no conducting paramagnet is interfaced with our (Ga,Mn)As film the SHE-STT mechanism is excluded by design.

Theory of the Berry curvature anti-damping spin-orbit torque

We start by deriving the intuitive picture of our Berry curvature anti-damping SOT based on the Bloch equation description of the carrier spin dynamics. In (Ga,Mn)As, the combination of the broken inversion symmetry of the zinc-blende lattice and strain can produce spin-orbit coupling terms in the Hamiltonian which are linear in momentum and have the Rashba symmetry, $H_R = \frac{\alpha}{\hbar}(\sigma_x p_y - \sigma_y p_x)$, or the Dresselhaus symmetry, $H_D = \frac{\beta}{\hbar}(\sigma_x p_x - \sigma_y p_y)$ (see Fig. 1a).[8–11] Here $\boldsymbol{\sigma}$ are the Pauli spin matrices, α and β represent the strength of the Rashba and Dresselhaus spin-orbit coupling, respectively, $p_{x,y}$ are the momenta in the epilayer plane, and $\hbar$ is the Planck constant. The interaction between carrier spins and magnetization is described by the exchange Hamiltonian term, $H_{ex} = J\boldsymbol{\sigma} \cdot \mathbf{M}$. In (Ga,Mn)As, $\mathbf{M}$ corresponds to the ferromagnetically ordered local moments on the Mn d-orbitals and J is the antiferromagnetic carrier–local moment kinetic-exchange constant.[41] The physical origin of our anti-damping SOT is best illustrated assuming for simplicity a 2D parabolic form of the spin-independent part of the total Hamiltonian, $H = \frac{p^2}{2m} + H_{R(D)} + H_{ex}$, and the limit of $H_{ex} \gg H_{R(D)}$. In equilibrium, the carrier spins are then approximately aligned with the exchange field, independent of their momentum. The origin of the SOT can be understood from solving the Bloch equations for carrier spins during the acceleration of the carriers in the applied electric field, i.e., between the scattering events. Let's define x-direction as the direction of the applied electric field $\mathbf{E}$. For $-\mathbf{M} \parallel \mathbf{E}$, the equilibrium effective magnetic field acting on the carrier spins, $\mathbf{s} = \frac{\boldsymbol{\sigma}}{2}$, due to the exchange term is,

$\mathbf{B}^{eq}_{eff} \approx (2JM, 0, 0)$, in units of energy. During the acceleration in the applied electric field, $\frac{dp_x}{dt} = eE_x$ (t is time and e carrier charge), and the effective magnetic field acquires a time-dependent y-component due to H_R for which $\frac{dB_{eff,y}}{dt} = \frac{2\alpha}{\hbar}\frac{dp_x}{dt}$, as illustrated in Fig. 1b. For small tilts of the spins from equilibrium, the Bloch equations $\frac{d\mathbf{s}}{dt} = \frac{1}{\hbar}(\mathbf{s} \times \mathbf{B}_{eff})$ yield, $s_x \approx s$, $s_y \approx s\frac{B_{eff,y}}{B^{eq}_{eff}}$, and

$$s_z \approx -\frac{\hbar s}{(B^{eq}_{eff})^2}\frac{dB_{eff,y}}{dt} = -\frac{s}{2J^2M^2}\alpha e E_x \; . \tag{1}$$

The non-equilibrium spin orientation of the carriers acquires a time and momentum independent s_z component.

As illustrated in Figs. 1b,c, s_z depends on the direction of the magnetization $\mathbf{M}$ with respect to the applied electric field. It has a maximum for $\mathbf{M}$ (anti)parallel to $\mathbf{E}$ and vanishes for $\mathbf{M}$ perpendicular to $\mathbf{E}$. For a general angle, $\theta_{\mathbf{M}-\mathbf{E}}$, between $\mathbf{M}$ and to $\mathbf{E}$ we obtain,

$$s_{z,\mathbf{M}} \approx \frac{s}{2J^2M^2}\alpha e E_x \cos\theta_{\mathbf{M}-\mathbf{E}} \; . \tag{2}$$

The total non-equilibrium spin polarization, $S_z = 2g_{2D}JMs_{z,\mathbf{M}}$, is obtained by integrating $s_{z,\mathbf{M}}$ over all occupied states (g_{2D} is the density of states). The non-equilibrium spin polarization produces an out-of-plane field which exerts a torque on the in-plane magnetization. From Eq. (2) we obtain that this intrinsic SOT is anti-damping-like,

$$\frac{d\mathbf{M}}{dt} = \frac{J}{\hbar}(\mathbf{M} \times S_z\hat{z}) \sim \mathbf{M} \times ([\mathbf{E} \times \hat{z}] \times \mathbf{M}) \, . \tag{3}$$

For the Rashba spin-orbit coupling, Eq. (3) applies to all directions of the applied electric field with respect to crystal axes. In the case of the Dresselhaus spin-orbit coupling, the symmetry of the anti-damping SOT depends on the direction of $\mathbf{E}$ with respect to crystal axes. In Table I we summarise the angle dependence of the Rashba and Dresselhaus contributions to S_z for electric fields along different crystal directions. (Note that in the case of the magnetization aligned in the out-of-plane direction, the Berry curvature non-equilibrium spin-polarization component will have an in-plane direction, with the in-plane angle depending on the form of the spin-orbit Hamiltonian and on the current direction.)

To highlight the analogy in microscopic mechanisms but also the distinct phenomenologies of our anti-damping SOT and the intrinsic Berry curvature SHE[28,29] we illustrate in Fig. 1d the solution of the Bloch equations in the absence of the exchange Hamiltonian term.[29] In this case $\mathbf{B}^{eq}_{eff}$ depends on the angle, $\theta_{\mathbf{p}}$, of the carrier momentum with respect to $\mathbf{E}$ which implies a momentum-dependent z-component of the non-equilibrium spin,

$$s_{z,\mathbf{p}} \approx \frac{s\hbar^2}{2\alpha p^2}\alpha e E_x \sin\theta_{\mathbf{p}} \ . \tag{4}$$

Clearly the same spin rotation mechanism which generates the uniform bulk spin accumulation in the case of our anti-damping SOT in a ferromagnet (Fig. 1b) is responsible for the scattering-independent spin-current of the SHE in a paramagnet (Fig. 1d). Note that the SHE spin-current yields zero spin accumulation in the bulk and a net spin-polarization can occur only at the edges of the paramagnet.

To complete the picture of the common origin between the microscopic physics of the Berry curvature SHE and our anti-damping SOT we point out that equivalent expressions for the SHE spin current and the SOT spin polarization can be obtained from the quantum-transport Kubo formula. The expression for the out-of-plane non-equilibrium spin polarization that generates our anti-damping SOT is given by

$$S_z = \frac{\hbar}{V}\sum_{\mathbf{k},a\neq b}(f_{\mathbf{k},a} - f_{\mathbf{k},b})\frac{\mathrm{Im}[\langle \mathbf{k},a|s_z|\mathbf{k},b\rangle\langle \mathbf{k},b|e\boldsymbol{E}\cdot\mathbf{v}|\mathbf{k},a\rangle]}{(E_{\mathbf{k},a} - E_{\mathbf{k},b})^2} \ , \tag{5}$$

where $\mathbf{k}$ is the wavevector, a, b are the band indices, $\mathbf{v}$ is the velocity oprator, V is the volume, and $f_{\mathbf{k},a}$ is the Fermi-Dirac distribution function corresponding to band energies $E_{\mathbf{k},a}$. This expression is analogous to Eq. (9) in Ref. 29 for the Berry curvature intrinsic SHE.

Measurement of the anti-damping spin-orbit torque in (Ga,Mn)As

Previous studies of the SOT in (Ga,Mn)As epilayers have focused in the scattering-related, field-like SOT generated by the in-plane component of the non-equilibrium spin-polarization of carriers.[8,9,11] We now discuss our low-temperature (6 K) experiments in which we identify the presence of the anti-damping SOT due to the out-of-pane component of the non-equilibrium spin density in our in-plane magnetized (Ga,Mn)As samples. We follow the methodology of several previous experiments[2,11] and use current induced ferromagnetic resonance (FMR) to investigate the magnitude and symmetries of the alternating fields responsible for resonantly driving the magnetisation. In our experiment, illustrated schematically in Fig. 2a, a signal generator drives a microwave frequency current through a 4 $\mu m \times 40$ μm micro-bar patterned from a 18 nm thick (Ga,Mn)As epilayer with nominal 5% Mn-doping. A bias tee is used to measure the dc voltage across the sample, which is generated according to Ohm's law due to the product of the oscillating magneto-resistance (during magnetisation precession) and the microwave current.[42] Solving the Landau-Lifshitz-Gilbert equation of motion for the magnetisation for a small excitation field vector $(h_x, h_y, h_z)\exp[i\omega t]$, where h_i are the components of the excitation field amplitude and ω is its frequency, we find dc voltages containing symmetric (V_S) and anti-symmetric (V_A) Lorentzian functions, shown in Fig. 2b. As the saturated magnetization of the sample is rotated, using $\theta_{\mathbf{M}-\mathbf{E}}$ to indicate the angle from the current/bar direction, the in-plane and out-of plane components of the excitation field are associated with V_S and V_A via:

$$V_S \propto h_z \sin 2\theta_{\mathbf{M}-\mathbf{E}} \ , \tag{6}$$

$$V_A \propto -h_x \sin\theta_{\mathbf{M}-\mathbf{E}} \sin 2\theta_{\mathbf{M}-\mathbf{E}} + h_y \cos\theta_{\mathbf{M}-\mathbf{E}} \sin 2\theta_{\mathbf{M}-\mathbf{E}} \ . \tag{7}$$

In this way we are able to determine, at a given magnetization orientation, the current induced field vector. In Fig. 2c we show the angle dependence of V_S and V_A for an in-plane rotation of the magnetization for a micro-bar patterned in the [100] crystal direction. As described in the Supplementary information note 1, the voltages V_S and V_A are related to the alternating excitation field, using the micro-magnetic parameters and anisotropic magnetoresistance of the sample. The in-plane field components, determined from V_A, are fitted by a M-independent current induced field vector ($\mu_0 h_x, \mu_0 h_y$)=(-91,-15) μTreferenced to a current density of 10^5 Acm^{-2} (μ_0 is the permeability of vacuum). Since V_S is non-zero, it is seen that there is also a significant h_z component of the current induced field. Furthermore, V_S is not simply described by $\sin 2\theta_{\mathbf{M}-\mathbf{E}}$ and, correspondingly, h_z depends strongly on the in-plane orientation of the magnetization. To analyse the symmetry of the out-of-plane field we fit the angle dependence of V_S, finding for the [100] bar shown in (Fig. 2c) that $\mu_0 h_z = (13 + 95\sin\theta_{\mathbf{M}-\mathbf{E}} + 41\cos\theta_{\mathbf{M}-\mathbf{E}})$ μT.

We show measurements of 8 samples, 2 patterned in each crystal direction and plot in Fig. 3 the resulting $\sin\theta_{\mathbf{M}-\mathbf{E}}$ and $\cos\theta_{\mathbf{M}-\mathbf{E}}$ coefficients of h_z. The corresponding in-plane fields are also shown: since these are approximately magnetisation-independent they can be represented in Fig. 3 by a single vector. In the [100] bar we found that the $\sin\theta_{\mathbf{M}-\mathbf{E}}$ coefficient of h_z, which according to the theoretical model originates in the Dresselhaus spin-orbit term, is greater than the $\cos\theta_{\mathbf{M}-\mathbf{E}}$ coefficient related to the Rashba spin-orbit term (see Table 1). If we examine the symmetries of h_z in our sample set, we find that they change in the manner expected for samples with dominant Dresselhaus term; a trend that is in agreement with the in-plane fields. The angle-dependence of h_z measured throughout our samples indicates an anti-damping like SOT with the theoretically predicted symmetries. Since the magnitude of the measured h_z is comparable to the in-plane fields (see Supplementary information table I for a detailed comparison), the anti-damping and field-like SOTs are equally important for driving the magnetisation dynamics in our experiment.

We note that the dominant Dresselhaus-like symmetry of h_z confirmed in a series of samples patterned along different crystal directions from the same or different (Ga,Mn)As wafers excludes that the measured V_S signals are artifacts of, e.g., sample inhomogeneities. The homogeneity of the micromagnetic parameters in our (Ga,Mn)As materials has been independently confirmed in a previous magneto-optical FMR study[43] and the driving field homogeneity in our SOT-FMR measurements has been discussed in the Supplementary Information of Ref. 11. The measurement artifacts of the frequency dependent phase-shifts between alternating electrical current and the FMR generating field in experiments with waveguides adjacent to the sample[44] are absent in our SOT-FMR devices in which the current and field are intrinsically linked. To confirm this, we performed SOT-FMR measurements over a range of different frequencies and observed a constant ratio, within experimental error, of the anti-symmetric and symmetric line-shapes (see Supplementary Information note 2). On the other hand we also note that the anti-damping SOT fields inferred from the V_S signals have a non-zero error bar whose magnitude can be associated with the fitted weaker constant terms shown in Fig. 3. These are also listed in table I of the Supplementary Information, showing that the constant terms, unlike the angle-dependent contributions, can fluctuate in amplitude and sign between nominally similar samples. We therefore attribute them to a random error from the measurement and fitting procedure.

Modelling of the anti-damping spin-orbit torque in (Ga,Mn)As

To model the measured anti-damping SOT, assuming its Berry curvature intrinsic origin, we start from the effective kinetic-exchange Hamiltonian describing (Ga,Mn)As:[41] $H = H_{\rm KL} + H_{\rm strain} + H_{\rm ex}$. We emphasize that the parameters of the Hamiltonian are taken to correspond to the measured (Ga,Mn)As samples and are not treated as free fitting parameters. $H_{\rm ex} = J_{\rm pd} c_{\rm Mn} S_{\rm Mn} \hat{\mathbf{M}} \cdot \mathbf{s}$, $H_{\rm KL}$ and $H_{\rm strain}$ refer to the strained Kohn-Luttinger

Hamiltonian for the hole systems of GaAs (see Supplementary Information note 3), $\mathbf{s}$ is the hole spin operator, $S_{\mathrm{Mn}} = 5/2$, c_{Mn} is the Mn density, and $J_{\mathrm{pd}} = 55$ meV nm^3 is the kinetic-exchange coupling between the localized d-electrons and the valence band holes. The Dresselhaus and Rashba symmetry parts of the strain Hamiltonian in the hole-picture are given by

$$H_{\mathrm{strain}} = -3C_4 \left[s_x \left(\epsilon_{yy} - \epsilon_{zz} \right) k_x + \mathrm{c.p.} \right] \\ -3C_5 \left[\epsilon_{xy} (k_y s_x - k_x s_y) + \mathrm{c.p.} \right], \tag{8}$$

where ϵ_{ij} are the strain components, $C_4 = 10$ eVÅ and we take $C_5 = C_4$.[45,46] These momentum-dependent H_{strain} terms are essential for the generation of SOT because they break the space-inversion symmetry. The momentum-dependent spin-orbit contribution to H_{KL} does not produce directly a SOT but it does interfere with the linear in-plane momentum terms in H_{strain} to reduce the magnitude of the SOT and introduce higher harmonics in the $\theta_{\mathbf{M}-\mathbf{E}}$ dependence of $\mu_0 h_z$. We have also performed additional calculations in which we replaced H_{KL} with a parabolic model with effective mass $m^* = 0.5 m_e$ (m_e is the bare electron mass) and included the spin-orbit coupling only through the Rashba and Dresselhaus-symmetry strain terms given by Eq. (8). The expected $\cos\theta_{\mathbf{M}-\mathbf{E}}$ or $\sin\theta_{\mathbf{M}-\mathbf{E}}$ symmetry without higher harmonics follows. In addition, a large increase of the amplitude of the effect is observed since the broken inversion symmetry spin-texture does not compete with the centro-symmetric one induced by the large spin-orbit coupled H_{KL} term. This indicates that for a system in which the dominant spin-orbit coupling is linear in momentum our Berry curvature anti-damping SOT will be largest.

In Fig. 4 we show calculations for our (Ga,Mn)As samples including the spin-orbit coupled H_{KL} term (full lines) term or replacing it with the parabolic model (dashed lines). The non-equilibrium spin density induced by the Berry curvature effect is obtained from the Kubo formula:[9]

$$S_z = \frac{\hbar}{2\pi V} \mathrm{Re} \sum_{\mathbf{k}, a \neq b} \langle \mathbf{k}, a | s_z | \mathbf{k}, b \rangle \langle \mathbf{k}, b | e\boldsymbol{E} \cdot \mathbf{v} | \mathbf{k}, a \rangle [G^A_{\mathbf{k}a} G^R_{\mathbf{k}b} - G^R_{\mathbf{k}a} G^R_{\mathbf{k}b}], \tag{9}$$

where the Green's functions $G^R_{\mathbf{k}a}(E)|_{E=E_F} \equiv G^R_{\mathbf{k}a} = 1/(E_F - E_{\mathbf{k}a} + i\Gamma)$, with the property $G^A = (G^R)^*$. E_F is the Fermi energy and Γ is the disorder induced spectral broadening, taken in the simulations to be 25 meV which is a typical inter-band scattering rate obtained for the weakly compensated (Ga,Mn)As materials in the first order Born approximation.[41] Note that in the disorder-free limit, Eq. (9) turns for our model into Eq. (5) introduced above. (See also the Supplementary Information note 3 and Ref. 9.) The relation between S_z and the effective magnetic field generating the Berry curvature SOT is given by $\mu_0 h_z = -(J_{\rm pd}/g\mu_{\rm B})S_z$, where $\mu_{\rm B}$ is the Bohr magneton, and $g = 2$ corresponds to the localized d-electrons in (Ga,Mn)As (for more details on the modeling see Supplementary Information note 3).

Results of our calculations are compared in Fig. 4 with experimental dependencies of h_z on $\theta_{\mathbf{M-E}}$ measured in the 4 micro-bar directions. As expected, the parabolic model calculations strongly overestimate the SOT field h_z. On the other hand, including the competing centro-symmetric $H_{\rm KL}$ term, which is present in the (Ga,Mn)As valence band, gives the correct order of magnitude of h_z as compared to experiment. Moreover, by including the $H_{\rm KL}$ term we can also explain the presence of higher harmonics in the $\theta_{\mathbf{M-E}}$ dependencies seen in experiment and reflecting the specific form of the carrier Hamiltonian in (Ga,Mn)As. This confirms that the experimentally observed anti-damping SOT is of the Berry curvature origin.

Conclusions for other systems

Learning from the analogy with the intrinsic anomalous Hall effect, first identified in (Ga,Mn)As and subsequently observed in a number of ferromagnets, we infer that our Berry curvature SOT is a generic phenomenon in spin-orbit coupled magnetic systems with broken space-inversion symmetry. In particular, we expect this anti-damping Berry curvature SOT to be present in ferromagnet/paramagnet bilayers systems with the broken structural inversion symmetry and that it can contribute in similar strength as the SHE-STT mechanism. The intrinsic SOT effect, identified in our work in the epilayer of (Ga,Mn)As with broken inversion-symmetry in the crystal structure and with the competing SHE-STT mechanism excluded by design, is associated with the out-of-plane non-equilibrium spin density S_z. Our model calculations in the 2D ferromagnet with Rashba spin-orbit coupling showed that S_z in the intrinsic SOT is proportional to the strength of the spin-orbit coupling and inverse proportional to the strength of the exchange-field of the ferromagnet. We can compare this dependence on the spin-orbit and exchange couplings with the phenomenology of the competing SHE-STT mechanism. Ref. 37 shows that the intrinsic SHE current is proportional to the strength of the spin-orbit coupling in the paramagnetic $4d$, $5d$ transition metals. The non-equilibrim spin-density generating the adiabatic (anti-damping) STT is proportional to the spin-density injection rate from the external polarizer and inverse proportional to the strength of the exchange field in the ferromagnet.[47–49] In the SHE-STT, the role of the spin-density injection rate from the external polarizer is played by the spin-current generated by the SHE in the paramagnet. For the intrinsic-SHE/anti-damping(adiabatic)-STT we can then conclude that it is generated by the non-equilibrium spin-polarization which is proportional to the spin-orbit strength in the paramagnet and inverse proportional to the exchange-field strength in the ferromagnet. For the intrinsic-SOT we inferred the same proportionality to the spin-orbit strength and inverse proportionality to the exchange-field strength, only the SOT is considered to act within a few atomic layers forming the broken inversion-symmetry interface. Due to proximity effects, however, the strength of the exchange-field on either side of the interface can be comparable to the exchange-field in the magnetic transition metal and the same applies to the respective strengths of the interface and the bulk-paramagnet spin-orbit coupling. Therefore the SOT and SHE-STT can provide two comparably strong intrinsic mechanisms driving the in-plane current-induced spin dynamics in these technologically important transition metal bilayers.

Methods and Materials

Materials: The 18 nm thick ($Ga_{0.95}$,$Mn_{0.05}$)As epilayer was grown on a GaAs [001] substrate by molecular beam epitaxy, performed at a substrate temperature of 230 C. It was subsequently annealed for 8 hours at 200 C. It has a Curie temperature of 132 K; a room temperature conductivity of 387 Ω^{-1}cm^{-1} which increases to 549 Ω^{-1}cm^{-1} at 5 K; and has a carrier concentration at 5 K determined by high magnetic field Hall measurement of 1.1×10^{21} cm^{-3}.

Devices: Two terminal microbars are patterned in different crystal directions by electron beam lithography to have dimensions of $4{\times}40$ μm. These bars have a typical low temperature resistance of 10 $k\Omega$ (table II in Supplementary Information).

Experimental procedure: A pulse modulated (at 789 Hz) microwave signal (at 11 GHz) with a source power of (20 dBm) is transmitted down to cryogenic temperatures using low-loss, low semi-rigid cables. The microwave signal is launched onto a printed circuit board patterned with a coplanar waveguide, and then injected into the sample via a bondwire. The rectification voltage, generated during microwave precession, is separated from the microwave circuit using a bias tee, amplified with a voltage amplifier and then detected with lock-in amplifier. All measurements are performed with the samples at 6 K.

Calibration of microwave current: The resistance of a (Ga,Mn)As micro-bar depends on temperature, and therefore on the Joule heating by an electrical current. First, the resistance change of the micro-bar due to Joule heating of a direct current is measured. Then, the resistance change is measured as a function of applied microwave power. We assume the same Joule heating (and therefore resistance change of the micro-bar) for the same direct and rms microwave currents, enabling us to calibrate the unknown microwave current against the known direct current.

For more details on the methods related to our SOT-FMR experiments and on our (Ga,Mn)As materials see Refs. 11,43 and the Supplementary Information therein.

Additional information

Supplementary information accompanies this paper at www.nature.com/naturenanotechnology. Reprints and permission information is available online at http://npg.nature.com/reprintsandpermissions/. Correspondence and requests for materials should be addressed to AJF (ajf1006@cam.ac.uk).

Author contributions

Theory and data modeling: TJ, EKV, LPZ, KV, JS; Materials: VN, RPC, BLG; Sample preparation: ACI; experiments and data analysis: HK, DF, JW, AJF; writing: TJ, AJF, HK, JS; project planning: TJ, AJF, JS, HK.

---

* Present address: London Centre for Nanotechnology, UCL, 17-19 Gordon Street, WC1H 0AH, UK

† Electronic address: `ajf1006@cam.ac.uk`

1 Miron, I. M. *et al.* Perpendicular switching of a single ferromagnetic layer induced by in-plane current injection. *Nature* **476**, 189-193 (2011).

[2] Liu, L. *et al.* Spin-torque switching with the giant spin Hall effect of tantalum. *Science* **336**, 555-558 (2012).

[3] Edelstein, V. M. Spin polarization of conduction electrons induced by electric current in two-dimensional asymmetric electron systems. *Solid State Commun.* **73**, 233-235 (1990).

[4] Bernevig, B. A. & Vafek, O. Piezo-magnetoelectric effects in p-doped semiconductors. *Phys. Rev.* **B 72**, 033203 (2005).

[5] Manchon, A. & Zhang, S. Theory of nonequilibrium intrinsic spin torque in a single nanomagnet. *Phys. Rev.* **B 78**, 212405 (2008).

[6] Manchon, A. & Zhang, S. Theory of spin torque due to spin-orbit coupling. *Phys. Rev.* **B 79**, 094422 (2009).

[7] Matos-Abiague, A. & Rodriguez-Suarez, R. L. Spin-orbit coupling mediated spin torque in a single ferromagnetic layer. *Phys. Rev.* **B 80**, 094424 (2009).

[8] Chernyshov, A. *et al.* Evidence for reversible control of magnetization in a ferromagnetic material by means of spin-orbit magnetic field. *Nature Phys.* **5**, 656-659 (2009).

[9] Garate, I. & MacDonald, A. H. Influence of a transport current on magnetic anisotropy in gyrotropic ferromagnets. *Phys. Rev.* **B 80**, 134403 (2010).

[10] Endo, M., Matsukura, F. & Ohno, H. Current induced effective magnetic field and magnetization reversal in uniaxial anisotropy (Ga,Mn)As. *Appl. Phys. Lett.* **97**, 222501 (2010).

[11] Fang, D. *et al.* Spin-orbit driven ferromagnetic resonance: A nanoscale magnetic characterisation technique. *Nature Nanotech.* **6**, 413-417 (2011).

[12] Miron, I. M. *et al.* Current-driven spin torque induced by the Rashba effect in a ferromagnetic metal layer. *Nature Mater.* **9**, 230-234 (2010).

[13] Pi, U. H. *et al.* Tilting of the spin orientation induced by Rashba effect in ferromagnetic metal layer. *Appl. Phys. Lett.* **97**, 162507 (2010).

[14] Hals, K. M. D., Brataas, A. & Tserkovnyak, Y. Scattering theory of charge-current-induced magnetization dynamics. *Europhys. Lett.* **90**, 47002 (2010).

[15] Miron, I. M. *et al.* Fast current-induced domain-wall motion controlled by the Rashba effect. *Nature Mater.* **10**, 419-423 (2011).

[16] Suzuki, T. *et al.* Current-induced effective field in perpendicularly magnetized Ta/CoFeB/MgO wire. *Appl. Phys. Lett.* **98**, 142505 (2011).

[17] Kim, K.-W., Seo, S.-M., Ryu, J., Lee, K.-J. & Lee, H.-W. Magnetization dynamics induced by

in-plane currents in ultrathin magnetic nanostructures with Rashba spin-orbit coupling. *Phys. Rev.* **B 85**, 180404(R) (2012).

[18] Pesin, D. A. & MacDonald, A. H. Quantum kinetic theory of current-induced torques in rashba ferromagnets. *Phys. Rev.* **B 86**, 014416 (2012).

[19] Wang, X. & Manchon, A. Diffusive spin dynamics in ferromagnetic thin films with a Rashba interaction. *Phys. Rev. Lett.* **108**, 117201 (2012).

[20] Manchon, A. Spin Hall effect versus Rashba torque: a diffusive approach (2012). arXiv:1204.4869.

[21] van der Bijl, E. & Duine, R. A. Current-induced torques in textured Rashba ferromagnets. *Phys. Rev.* **B 86**, 094406 (2012).

[22] Kim, J. *et al.* Layer thickness dependence of the current-induced effective field vector in Ta—CoFeB—MgO. *Nature Mater.* **12**, 240-245 (2012).

[23] Garello, K. *et al.* Symmetry and magnitude of spin-orbit torques in ferromagnetic heterostructures. *Nature Nanotech.* **8**, 587-593 (2013).

[24] Li, H., Wang, X., Dogan, F. & Manchon, A. Tailoring spin-orbit torque in diluted magnetic semiconductors. *Appl. Phys. Lett.* **102**, 192411 (2013).

[25] Liu, L., Lee, O. J., Gudmundsen, T. J., Ralph, D. C. & Buhrman, R. A. Current-induced switching of perpendicularly magnetized magnetic layers using spin torque from the spin Hall effect. *Phys. Rev. Lett.* **109**, 096602 (2011).

[26] Dyakonov, M. I. & Perel, V. I. Current-induced spin orientation of electrons in semiconductors. *Phys. Lett. A* 459-460 (1971).

[27] Hirsch, J. E. Spin Hall effect. *Phys. Rev. Lett.* **83**, 1834-1837 (1999).

[28] Murakami, S., Nagaosa, N. & Zhang, S.-C. Dissipationless quantum spin current at room temperature. *Science* **301**, 1348-1351 (2003).

[29] Sinova, J. *et al.* Universal intrinsic spin Hall effect. *Phys. Rev. Lett.* **92**, 126603 (2004).

[30] Kato, Y. K., Myers, R. C., Gossard, A. C. & Awschalom, D. D. Observation of the spin Hall effect in semiconductors. *Science* **306**, 1910-1913 (2004).

[31] Wunderlich, J., Kaestner, B., Sinova, J. & Jungwirth, T. Experimental observation of the spin Hall effect in a two dimensional spin-orbit coupled semiconductor system. *Phys. Rev. Lett.* **94**, 047204 (2005).

[32] Jungwirth, T., Wunderlich, J. & Olejnik, K. Spin Hall effect devices. *Nature Mater.* **11**, 382-390

(2012).

[33] Slonczewski, J. C. Current-driven excitation of magnetic multilayers. *J. Magn. Magn. Mater.* **159**, L1-L7 (1996).

[34] Berger, L. Emission of spin waves by a magnetic multilayer traversed by a current. *Phys. Rev.* **B 54**, 9353-9358 (1996).

[35] D. Ralph and M. Stiles and S. Bader (editors). Current perspectives: Spin transfer torques. *J. Magn. Magn. Mater.* **320**, 1189-1311 (2008).

[36] Brataas, A., Kent, A. D. & Ohno, H. Current-induced torques in magnetic materials. *Nature Mater.* **11**, 372-381 (2012).

[37] Tanaka, T. *et al.* Intrinsic spin Hall effect and orbital Hall effect in 4d and 5d transition metals. *Phys. Rev.* **B 77**, 165117 (2008).

[38] Engel, H.-A., Rashba, E. I. & Halperin, B. I. Out-of-plane spin polarization from in-plane electric and magnetic fields. *Phys. Rev. Lett.* **98**, 036602 (2007).

[39] Jungwirth, T., Niu, Q. & MacDonald, A. H. Anomalous Hall effect in ferromagnetic semiconductors. *Phys. Rev. Lett.* **88**, 207208 (2002).

[40] Nagaosa, N., Sinova, J., Onoda, S., MacDonald, A. H. & Ong, N. P. Anomalous Hall effect. *Rev. Mod. Phys.* **82**, 1539-1592 (2010).

[41] Jungwirth, T., Sinova, J., Mašek, J., Kučera, J. & MacDonald, A. H. Theory of ferromagnetic (III,Mn)V semiconductors. *Rev. Mod. Phys.* **78**, 809-864 (2006).

[42] Tulapurkar, A. A. *et al.* Spin-torque diode effect in magnetic tunnel junctions. *Nature* **438**, 339-342 (2005).

[43] Nemec, P. *et al.* The essential role of carefully optimized synthesis for elucidating intrinsic material properties of (Ga,Mn)As. *Nat. Commun.* **4**, 1422 (2013).

[44] Harder, M., Cao, Z. X., Gui, Y. S., Fan, X. L. & Hu, C. M. Analysis of the line shape of electrically detected ferromagnetic resonance. *Phys. Rev.* **B 84**, 054423 (2011).

[45] Silver, M., Batty, W., Ghiti, A. & OReilly, E. P. Strain-induced valence-subband splitting in III-V semiconductors. *Physica* **B 46**, 6781-6788 (1992).

[46] Stefanowicz, W. *et al.* Magnetic anisotropy of epitaxial (Ga,Mn)As on (113)a GaAs. *Phys. Rev.* **B 81**, 155203 (2010).

[47] Vanhaverbeke, A. & Viret, M. Simple model of current-induced spin torque in domain walls. *Phys. Rev.* **B 75**, 024411 (2007).

[48] Fernández-Rossier, J., Núñez, A. S., Abolfath, M. & MacDonald, A. H. Optical spin transfer in ferromagnetic semiconductors (2003). arXiv:cond-mat/0304492.

[49] Nemec, P. *et al.* Experimental observation of the optical spin transfer torque. *Nature Phys.* **8**, 411-415 (2012).

Acknowledgment

We acknowledge fruitful discussions with, and support from EU ERC Advanced Grant No. 268066, from the Ministry of Education of the Czech Republic Grant No. LM2011026, from the Academy of Sciences of the Czech Republic Praemium Academiae, and from U.S. grants ONR-N000141110780, NSF-DMR-1105512 and NSF TAMUS LSAMP BTD Award 1026774. AJF acknowledges support from a Hitachi research fellowship. HK acknowledges financial support from the JST.

	Rashba: $S_z \sim$	Dresselhaus: $S_z \sim$
$\mathbf{E} \parallel [100]$	$\cos\theta_{\mathbf{M-E}}$	$\sin\theta_{\mathbf{M-E}}$
$\mathbf{E} \parallel [010]$	$\cos\theta_{\mathbf{M-E}}$	$-\sin\theta_{\mathbf{M-E}}$
$\mathbf{E} \parallel [110]$	$\cos\theta_{\mathbf{M-E}}$	$\cos\theta_{\mathbf{M-E}}$
$\mathbf{E} \parallel [1-10]$	$\cos\theta_{\mathbf{M-E}}$	$-\cos\theta_{\mathbf{M-E}}$

TABLE I: Angle $\theta_{\mathbf{M-E}}$ dependence of the Rashba and Dresselhaus contributions to S_z for electric fields along different crystal directions.

FIG. 1: **Spin-orbit coupling and anti-damping SOT. a,** Rashba (red) and Dresselhaus (blue) fields for momenta along different crystallographic directions. **b,** The semi-transparent regions represent the equilibrium configuration in which the carrier spins experience an equilibrium effective field $\mathbf{B}^{\mathbf{eq}}_{\mathbf{eff}}$, which anti-aligns them to the magnetisation, $\mathbf{M}$. During the acceleration by the applied electric field, $\mathbf{E}$, which shifts the centre of the Fermi surface by $\Delta\mathbf{p} \sim e\mathbf{E}t$ (blue arrow to dotted line), an additional field $\Delta\mathbf{B}_{\mathbf{eff}} \perp \mathbf{M}$ (purple arrows) is felt. This field causes all spins to tilt in the same out-of-plane direction. For the case of a Rashba-like symmetry, the out-of-plane non-equilibrium carrier spin-density that generates the Berry curvature anti-damping SOT has a maximum for an applied electric field (anti-)parallel to the magnetisation. **c,** For the case of a Rashba-like symmetry, the out-of-plane non-equilibrium carrier spin-density is zero for $\mathbf{E} \perp \mathbf{M}$ since $\mathbf{B}^{\mathbf{eq}}_{\mathbf{eff}}$ and $\Delta\mathbf{B}_{\mathbf{eff}}$ are parallel to each other. **d,** The analogous physical phenomena for zero magnetization induces a tilt of the spin out of the plane that has opposite sign for momenta pointing to the left or the right of the electric field, inducing in this way the intrinsic Berry curvature SHE.[29]

FIG. 2: **Spin-orbit FMR experiment.** **a,** Schematic of the sample, measurement setup and magnetisation precession. Microwave power goes through a bias-tee and into the (Ga,Mn)As micro-bar which is placed inside a cryostat. The injected microwave current drives FMR that is detected via a dc voltage $V_{\rm dc}$ across the micro-bar. We define $\theta_{\mathbf{M}-\mathbf{E}}$ as an angle of the static magnetisation direction determined by the external magnetic field, measured from the current flow direction. The arrows represent in-plane (blue) and out-of-plane (red) components of the instantaneous non-equilibrium spin polarisation induced by the microwave current which drives the magnetisation. **b,** Typical spin-orbit FMR signal driven by an alternating current at 11 GHz and measured by $V_{\rm dc}$ as a function of external magnetic field. The data were fitted by a combination of symmetric and anti-symmetric Lorentzian functions. **c,** Symmetric (blue data points and fitted line) and antisymmetric (red data points and fitted line) component of $V_{\rm dc}$ as a function of $\theta_{\mathbf{M}-\mathbf{E}}$ for current along the [100] direction.

FIG. 3: **In-plane and out-of-plane SOT fields.** **a,** Direction and magnitude of the in-plane spin-orbit field (blue arrows) within the micro-bars (light-blue rectangles). A single sample in each micro-bar direction is shown (corresponding to the same samples that yield the blue out-of-plane data points). **b,** Coefficients of the $\cos\theta_{\mathbf{M}-\mathbf{E}}$ and $\sin\theta_{\mathbf{M}-\mathbf{E}}$ fits to the angle-dependence of out-of-plane SOT field for our sample set. In this out-of-plane data, 2 samples are shown in each micro-bar direction. The symmetries expected for the anti-damping SOT, on the basis of the theoretical model for the Dresselhaus term in the spin-orbit interaction, are shown by light green shading. All data are normalised to a current density of 10^5 Acm^{-2}.

FIG. 4: **Theoretical modeling of the measured angular dependencies of the SOT fields.** Microscopic model calculation for the measured (Ga,Mn)As samples assuming Rashba ($\epsilon_{xy} = -0.15\%$) and Dresselhaus ($\epsilon_{xx} = -0.3\%$) strain. Solid blue lines correspond to the calculations with the centro-symmetric $H_{\rm KL}$ term included in the (Ga,Mn)As Hamiltonian. Dashed blue lines correspond to replacing $H_{\rm KL}$ with the parabolic model. Both calculations are done with a disorder broadening $\Gamma = 25$ meV. Black points are experimental data whose fitting coefficients of the $\cos\theta_{\mathbf{M}-\mathbf{E}}$ and $\sin\theta_{\mathbf{M}-\mathbf{E}}$ first harmonics correspond to blue points in Fig. 3.

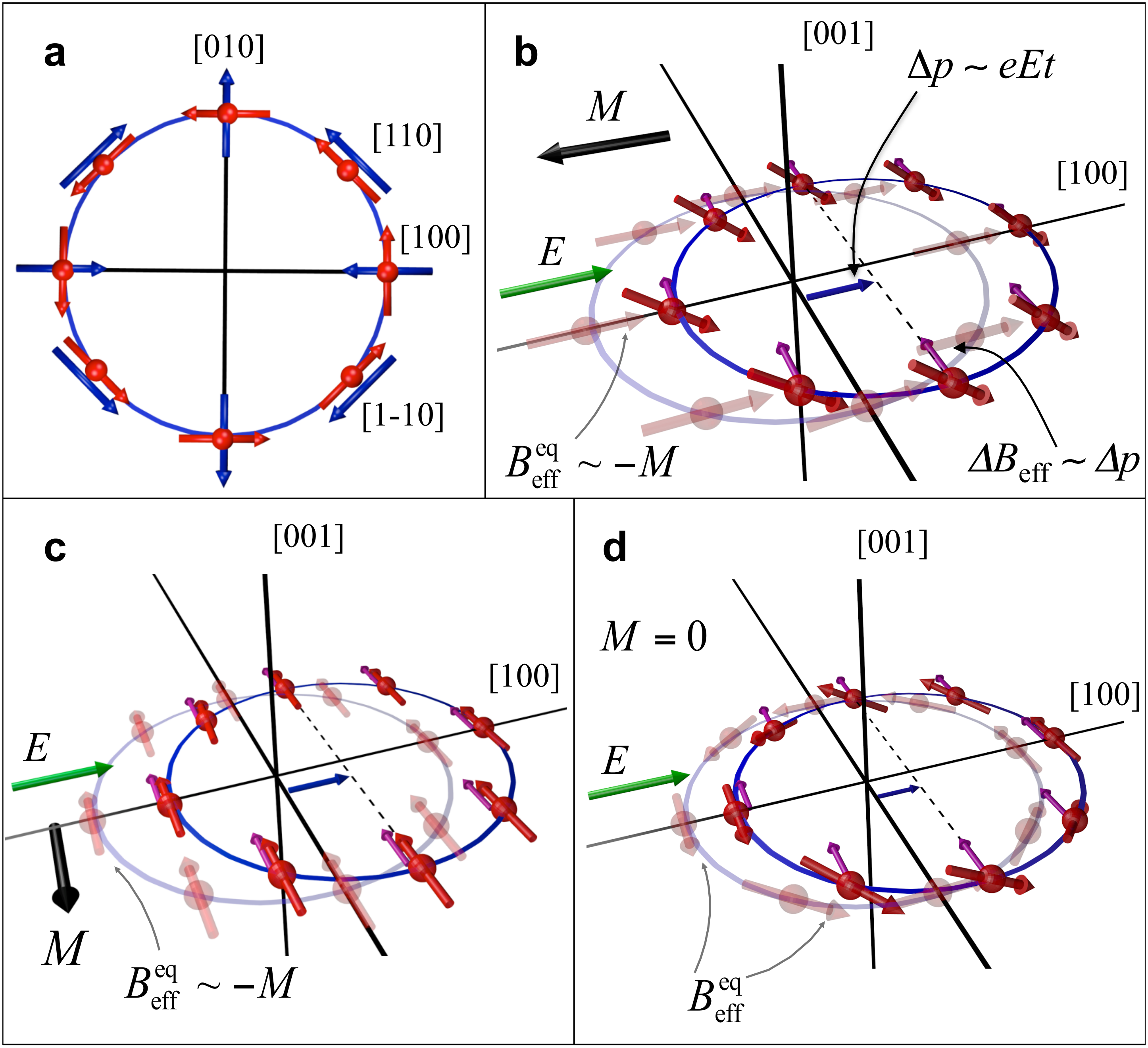

a
[010]
[110]
[100]
[1-10]
b
[001]
$\Delta p \sim eEt$
M
[100]
E
$B_{\mathrm{eff}}^{\mathrm{eq}} \sim -M$
$\Delta B_{\mathrm{eff}} \sim \Delta p$
c
[001]
[100]
E
M
$B_{\mathrm{eff}}^{\mathrm{eq}} \sim -M$
d
[001]
$M = 0$
[100]
E
$B_{\mathrm{eff}}^{\mathrm{eq}}$

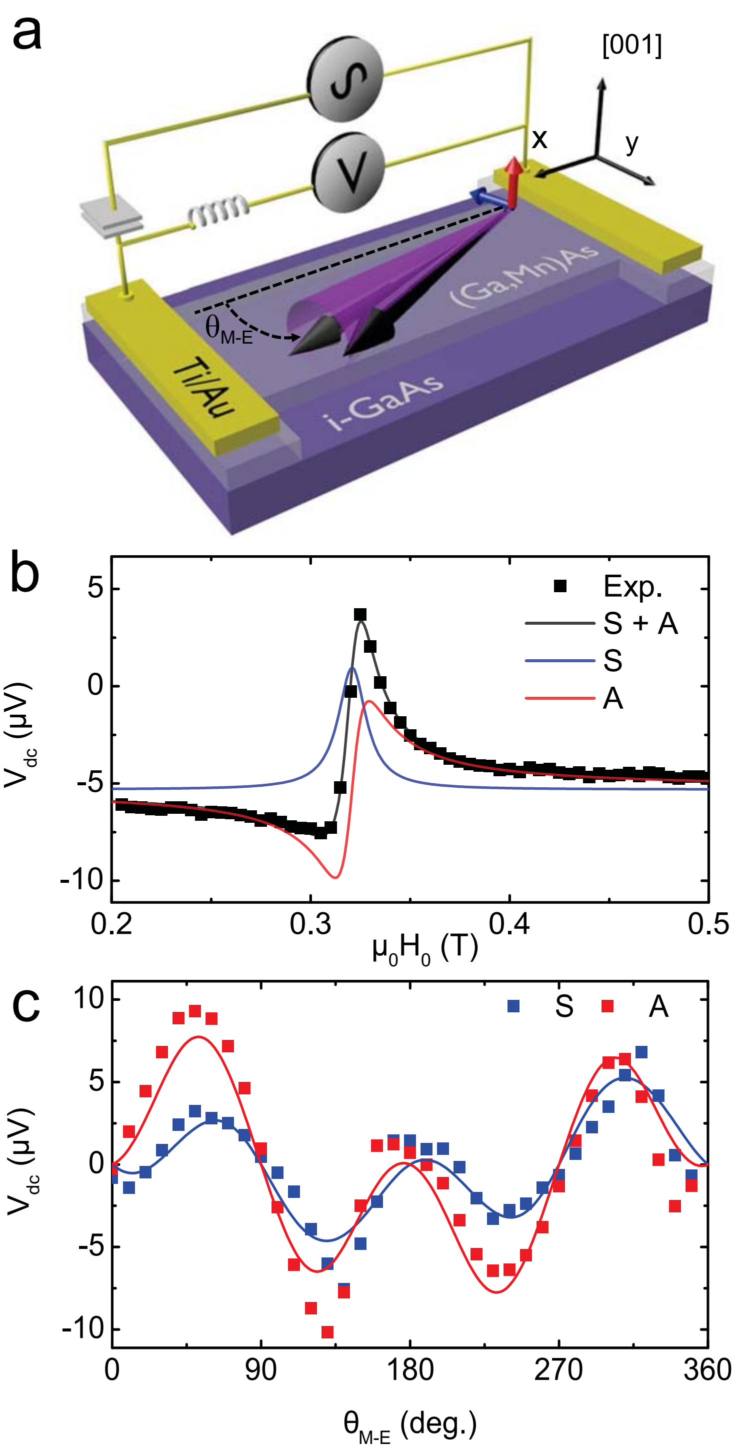
a
[001]
x
y
(Ga,Mn)As
θM-E
Ti/Au
i-GaAs
b
Exp.
S + A
S
A
Vdc (μV)
μ0H0 (T)
c
S
A
Vdc (μV)
θM-E (deg.)

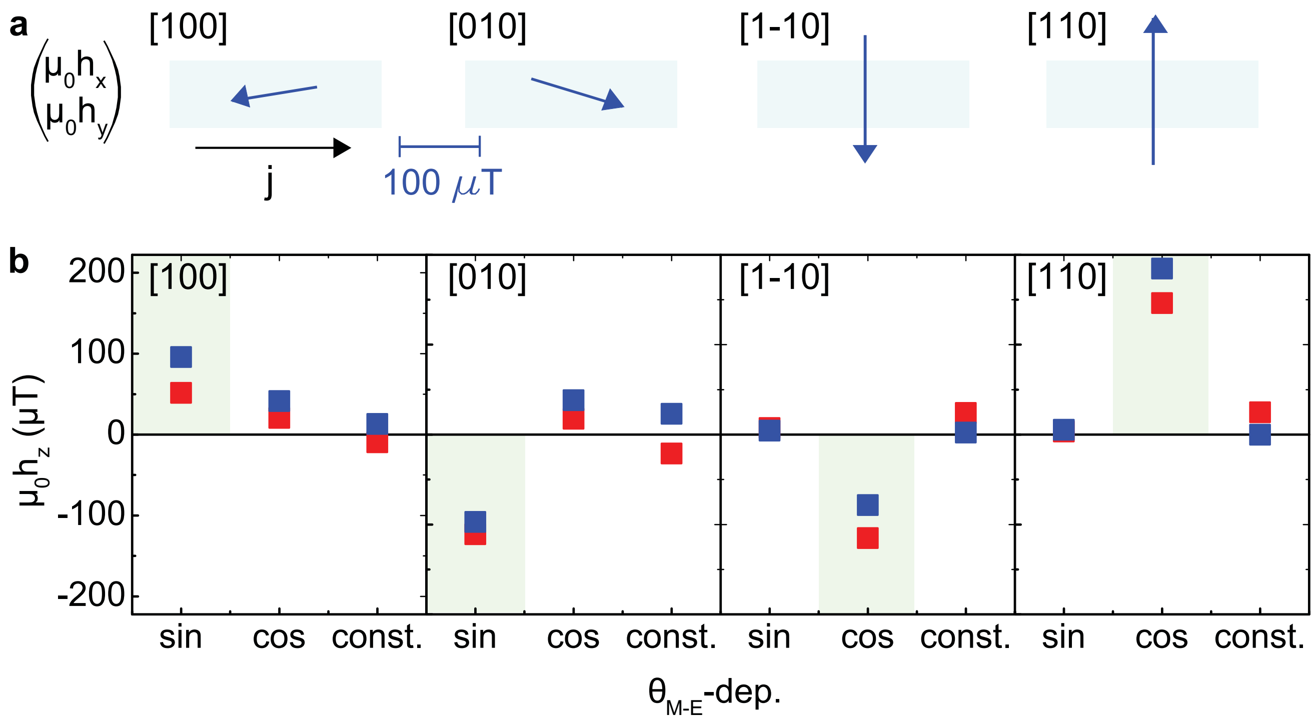

a
[100]
[010]
[1-10]
[110]
μ0hx
μ0hy
j
100 μT
b
[100]
[010]
[1-10]
[110]
200
100
0
-100
-200
μ0hz (μT)
sin
cos
const.
sin
cos
const.
sin
cos
const.
sin
cos
const.
θM-E-dep.

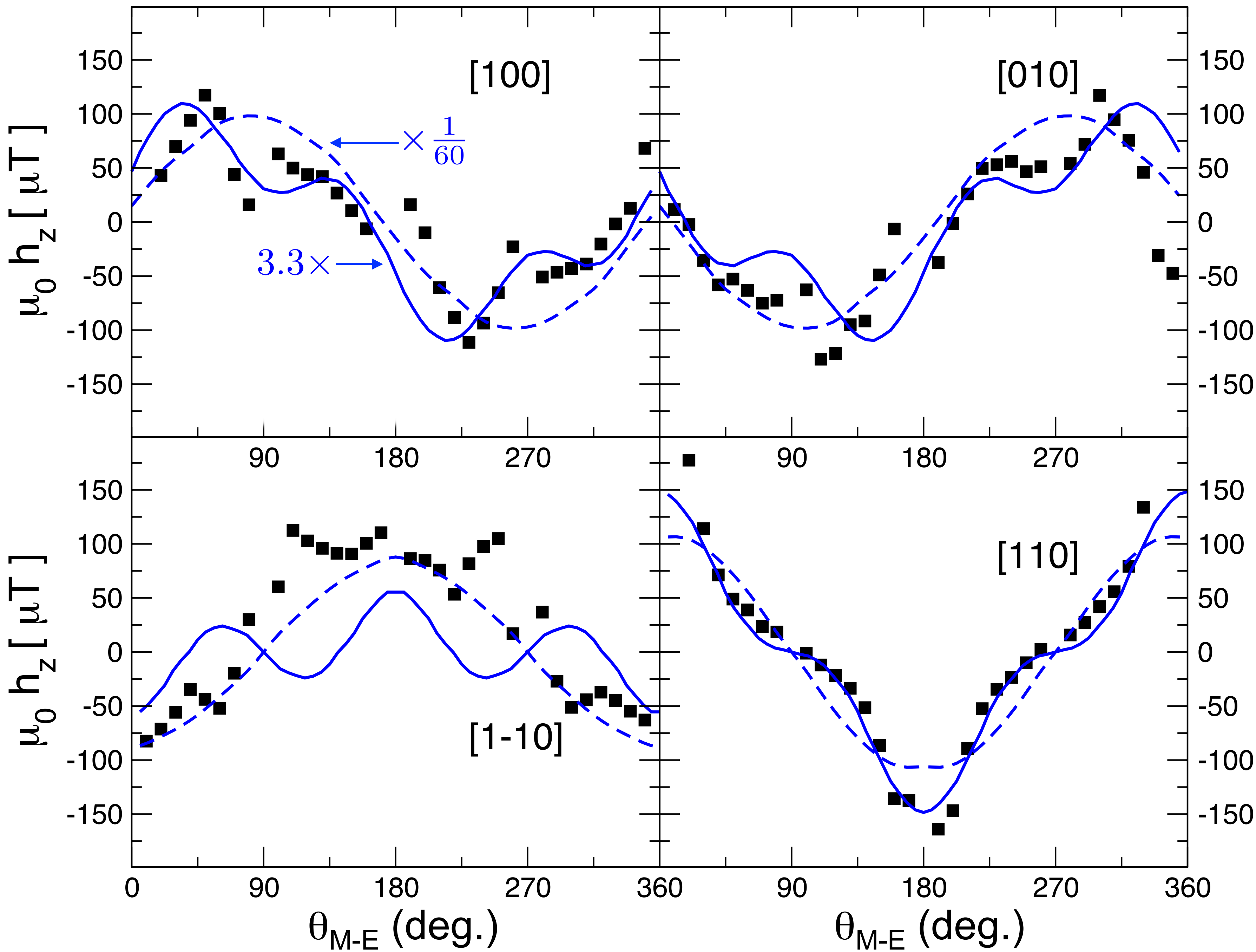
[100]
[010]
[1-10]
[110]
× 1/60
3.3×
μ0 hz [μT]
θM-E (deg.)
150
100
50
0
-50
-100
-150
0
90
180
270
360